

# TRIAXIAL BLACK-HOLE NUCLEI

M. Y. POON & D. MERRITT

Department of Physics and Astronomy, Rutgers University, New Brunswick, NJ 08855

*Draft version December 2, 2024*

## ABSTRACT

We demonstrate that the nuclei of galaxies containing supermassive black holes can be triaxial in shape. Schwarzschild’s method was first used to construct self-consistent orbital superpositions representing nuclei with axis ratios of 1 : 0.79 : 0.5 and containing a central point mass representing a black hole. Two different density laws were considered,  $\rho \propto r^{-\gamma}$ ,  $\gamma = \{1, 2\}$ . Only non-chaotic orbits were used in the solutions and the main contribution to the density was found to come from tube orbits which avoid the central singularity. Monte-Carlo realizations of the models were then advanced in time using an  $N$ -body code to verify their stability. Both models were found to retain their triaxial shapes for many crossing times. The possibility that galactic nuclei may be triaxial complicates the interpretation of stellar-kinematical data from the centers of galaxies and may alter the inferred interaction rates between stars and supermassive black holes.

Keywords: galaxies: elliptical and lenticular — galaxies: structure — galaxies: nuclei — stellar dynamics

## 1. INTRODUCTION

The phenomenon of triaxiality has remained of central importance to our understanding of galaxy dynamics since the demonstration by Schwarzschild (1979, 1982) of the existence of self-consistent triaxial equilibria. Schwarzschild’s models had large, constant-density cores and the majority of the orbits were regular, respecting three integrals of the motion. But the realization that the central densities of elliptical galaxies and bulges are very high (Crane et al. 1993), and that supermassive black holes are generic components of galaxies (Kormendy & Richstone 1995), has modified somewhat our ideas about the persistence of triaxiality. A central black hole can destroy triaxiality on large scales by rendering the center-filling box orbits stochastic (Gerhard & Binney 1985). Evolution to globally axisymmetric shapes can occur in just a few crossing times if the black hole contains of order  $10^{-2}$  of the galaxy’s mass (Merritt & Quinlan 1998; Sellwood 2001).

Less is known about the possibility of maintaining triaxial shapes at the very centers of galaxies, where the gravitational force is contributed roughly equally by the stars and by the nuclear black hole. Regular orbits, both box-like and tube-like, exist in this region (Merritt & Valluri 1999; Sambhus & Sridhar 2000; Poon & Merritt 2001, Paper I) but the box-like orbits (the “pyramids”) have shapes that are generally contrary to the figure elongation, making them less useful than classical box orbits for maintaining a triaxial shape. Furthermore the pyramid orbits disappear within the “zone of chaos,” which begins at a radius where the enclosed stellar mass is a few times that of the black hole (Paper I), roughly  $10^2$  pc in a typical bright elliptical galaxy, and extends outward to a radius containing  $\sim 10^2 M_{bh}$ . Stable triaxial equilibria, if they exist in and below the zone of chaos, would need to be supported by orbits that have favorable shapes and that avoid the destabilizing central singularity.

Here we demonstrate that triaxial equilibria do in fact

exist in the vicinity of the black hole. We first (§2) use Schwarzschild’s technique to construct self-consistent superpositions of orbits computed in a fixed triaxial potential representing the stars and a central point mass representing a supermassive black hole. We then (§3) test the long-term stability of the models by using an  $N$ -body code to advance them forward in time; we find that the  $N$ -body models maintain their triaxial shapes for many crossing times. Finally we present some of the observable properties of the models (§4) and discuss the implications of triaxiality for observational and theoretical studies of galactic nuclei (§5).

## 2. SCHWARZSCHILD SOLUTIONS

We model the stellar nucleus as a triaxial spheroid with a power-law dependence of density on radius,

$$\rho_\star = \rho_\circ m^{-\gamma}, \quad (1a)$$

$$m = \sqrt{\frac{x^2}{a^2} + \frac{y^2}{b^2} + \frac{z^2}{c^2}}, \quad (1b)$$

inside of some surface  $m = m_{out}$  discussed below. We took  $\gamma = 1$  or 2; these values correspond roughly to the density profiles observed at the centers of bright and faint elliptical galaxies, respectively (Gebhardt et al. 1996). The triaxiality  $T$  is defined as

$$T \equiv \frac{a^2 - b^2}{a^2 - c^2}. \quad (2)$$

We chose  $a = 1.0, b = 0.79, c = 0.5$  for both models, corresponding to  $T = 0.5$ , “maximal” triaxiality. The central black hole is represented by a point mass with  $M_{bh} = 1$ . Expressions for the gravitational potential and forces corresponding to this mass model are given in Paper I.

Although our mass model for the stars is scale-free, the presence of the black hole imposes a scale. We identify three characteristic radii associated with the black hole. At a radius of  $r_g$ , the enclosed mass in stars (defined as the mass within an equidensity surface which intersects

the  $x$ -axis at  $x = r_g$ ) is equal to that of the black hole. In real galaxies,  $r_g$  is typically a factor of  $\sim$  a few greater than the “sphere of influence”  $r_h$ , where

$$r_h \equiv \frac{GM_{bh}}{\sigma_*^2} \approx 10.8 \text{ pc} \left( \frac{M_{bh}}{10^8 M_\odot} \right) \left( \frac{\sigma_*}{200 \text{ km s}^{-1}} \right)^{-2} \quad (3)$$

depends on the stellar velocity dispersion  $\sigma_*$ . The third fiducial radius is  $r_{ch}$ , the radius at which the character of the box-like orbits undergoes a sudden transition to chaos in triaxial potentials. Table 1 gives values of  $r_g$  and  $r_{ch}$  for our two mass models; values of  $r_{ch}$  are approximate and are taken from Paper I. Table 1 also gives values of the dynamical times at  $r_g$  and  $r_{ch}$ , defined as the period of a circular orbit of the same energy in the equivalent spherical potential, defined to have a scale length  $a_{ave} = (abc)^{1/3}$ . The enclosed stellar mass within  $r_{ch}$  is about  $3M_{bh}$  for  $\gamma = 1$  and  $6M_{bh}$  for  $\gamma = 2$ .

TABLE 1

	$\gamma = 1$	$\gamma = 2$
$r_g$	0.64	0.20
$T_D(r_g)$	0.98	0.17
$r_{ch}$	1.1	1.3
$T_D(r_{ch})$	1.8	1.5
$m_{out}$	5.6	3.8
$T_D(m_{out})$	5.1	4.6

Any numerical realization of a stellar system must have an outer boundary. In the case of models constructed via orbital superposition, a choice must be made whether or not to allow orbits to extend beyond this surface. Doing so may yield solutions in which the density undergoes an unphysical jump; including only orbits that lie within the outer boundary limits the ability to reproduce the density in the outermost shells. This problem is particularly acute when the density is slowly decaying at the outer edge, as in our  $\gamma = 1$  model, since a large fraction of the density near the boundary would be expected to come from orbits outside of the region under consideration.

We chose to test self-consistency out to a radius of roughly  $r_{ch}$ , corresponding to  $\sim 2r_g$  for  $\gamma = 1$  and  $\sim 6r_g$  for  $\gamma = 2$ . We therefore chose the outer surface of our mass model,  $m = m_{out}$ , to be large enough that almost all of the density at  $r_{ch}$  in a real galaxy would be contributed by orbits with apocenters below this surface. In order to estimate  $m_{out}$ , the isotropic distribution functions corresponding to a spherical galaxy with the density law of equation (1),  $\gamma = \{1, 2\}$ , and a central point mass were computed and transformed to  $F(r_{apo}; r)$ , the distribution of apocentric radii  $r_{apo}$  of orbits passing through  $r$ . For  $\gamma = 1$ , we found that orbits with  $r_{apo} \lesssim 5r_{ch}$  contribute  $\sim 70\%$  of the density at  $r_{ch}$ . For  $\gamma = 2$ , setting  $r_{apo} \approx 3r_{ch}$  is sufficient to give  $\sim 75\%$  of the density at  $r_{ch}$ . ( $r_{ch}$  in the spherical models was defined as the radius containing the same mass as in the triaxial models.) Our corresponding choices for  $m_{out}$  are given in Table 1.

We followed standard procedures for constructing the Schwarzschild solutions (Schwarzschild 1993; Merritt & Fridman 1996). The mass model within  $m_{out}$  was divided into 64 equidensity shells and each shell was divided into

48 cells per octant, for a total of 3072 cells. Shells were more closely spaced near the center (Figure 1). Orbits were computed in two initial condition spaces: stationary start space, which yields box-like orbits, and  $X - Z$  start space, which yields mostly tube orbits. Orbital energies were selected from a grid of 42(52) values for  $\gamma = 1(2)$ , defined as the energies of equipotential surfaces that were spaced similarly in radius to the equidensity shells. The outermost energy shell intersected the  $x$  axis at  $x = m_{out}$  for both models. Orbits were integrated for 100 dynamical times, as defined above, and their contributions to the masses in the cells were recorded. In order to distinguish regular from stochastic trajectories, the largest Liapunov exponent was computed for each orbit. For  $\gamma = 1$ , the total number of orbits integrated was 18144 of which 9751 were found to be regular. For  $\gamma = 2$ , the numbers were 22464 and 15048 respectively. Orbital weights that reproduced the masses in the 3072 cells were found via quadratic programming (e.g. Dejonghe 1989).

As expected, orbital superpositions that exactly reproduced the cell masses in all of the cells, including the outermost ones, could not be found since only a few orbits visit the outer shells. We were able to find “exact” solutions (solutions which accurately reproduced the densities in a subset of cells) by relaxing the constraints in a number of ways; for instance, by eliminating the angular constraints on the outermost shells (forcing only the integrated shell mass to be fit), or by ignoring the outer cells entirely when imposing the constraints. For example, when only regular orbits were included, “exact” solutions could be found for  $\gamma = 1$  for all cells within shell 51, corresponding to a radius of  $\sim 3.2$ . This radius is substantially greater than  $r_{ch}$  (Table 1).

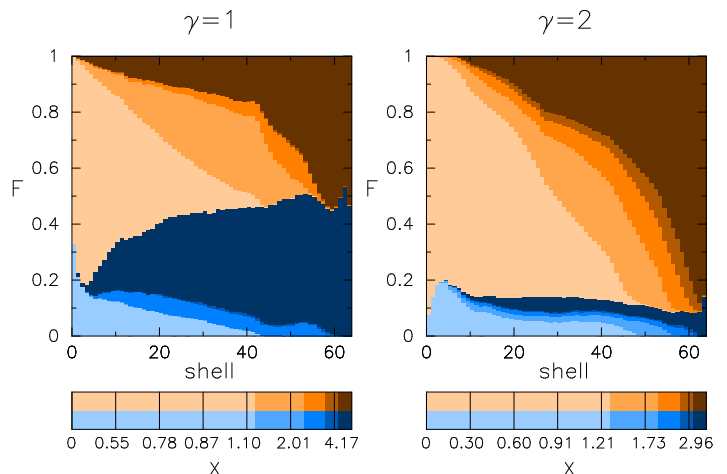


FIG. 1.— Cumulative mass fractions  $F$  contributed by different kinds of orbits to different shells of the triaxial models. Box-like orbits are blue and tube orbits (both  $z$ - and  $x$ -tubes) are orange. Higher energies are indicated via darker shades; the color bar relates the shade to the radius of the equipotential surface, as explained in the text. Numbers below the color bar indicate radii where the equidensity shells intersect the  $x$ -axis.

When these “exact” solutions were advanced forward in time, as described below, they were found to exhibit significant evolution at large radii, due to the fact that the model’s density was not correctly reproduced in the outermost cells. We therefore constructed new solutions which were not “exact,” but which were constrained to reproduce

the densities in all cells within  $m_{out}$  with as high an accuracy as possible. These solutions had a typical, fractional error in the cell mass of  $\sim 6\%$ ; the error was close to zero for the innermost cells,  $r \lesssim r_{ch}$ , and increased outward. Models constructed in this way were found to evolve much less than the “exact” solutions and provide the basis for the discussion below.

The orbital content of the latter solutions is given in Table 2. The dominant family of orbits in both models was found to be the  $z$ -tubes, orbits which circulate about the short axis of the figure.  $z$ -tube orbits contribute  $\sim 55\%$  of the mass within  $r_{ch}$  in the  $\gamma = 1$  model and  $\sim 73\%$  of the mass within  $r_{ch}$  in the  $\gamma = 2$  model. The contribution of the  $z$ -tubes is roughly constant with radius. Plots of the individual orbits used in the solutions show that many of the  $z$ -tubes have the correct shape for reproducing the triaxial figure, being more elongated in  $x$  (the long axis) than in  $y$  (the intermediate axis). Most of the remaining contribution to the density was found to come from pyramid orbits and high-energy box orbits in the  $\gamma = 1$  model, while for  $\gamma = 2$ , roughly equal contributions came from pyramid orbits and from the  $x$ -tubes. (See Paper I, Figure 1 for illustrations of the various orbit families.) The most heavily occupied pyramid orbits had shapes similar to “saucer” orbits,  $z$ -tubes associated with a 2 : 1 resonance (Paper I, Figure 1c); both models contained roughly equal numbers of saucers and pyramids. High-energy box-like orbits are much more important in the  $\gamma = 1$  case than in the  $\gamma = 2$  case, because : 1) high-energy tube orbits in the  $\gamma = 1$  model are elongated opposite to the figure; 2) most of the regular box orbits in the  $\gamma = 2$  model are bananas, which are not very useful for filling the outermost shells.

TABLE 2

	$z$ -tubes	$x$ -tubes	Pyramids
$\gamma = 1$ :			
$r < 0.5$	0.61	0.10	0.29
$r < 1.0$	0.56	0.08	0.37
$r < 1.5$	0.53	0.07	0.40
$\gamma = 2$ :			
$r < 0.4$	0.75	0.10	0.15
$r < 0.8$	0.73	0.13	0.14
$r < 1.2$	0.73	0.13	0.13

Cumulative mass fractions contributed by different types of orbit as a function of their energy are shown in Figure 1. Blue colors represent orbits from stationary start space (mostly pyramids) while orange colors represent tube orbits. Darker shades represent orbits with higher energies, defined according to the  $x$ -intercept of the equipotential which has the same energy as the orbit. For example, box orbits with energy equal to  $\Phi(0.78, 0.0, 0.0)$  are represented by the lightest blue color for  $\gamma = 1$ .

### 3. N-BODY MODELS

Models constructed via Schwarzschild’s method may not represent true equilibria, for several reasons: discreteness effects, failure to exactly reproduce the densities in some or all of the cells, incorrect implementation of the quadratic programming algorithm, etc. We verified that our Schwarzschild solutions correspond to true equilibria

by realizing them as  $N$ -body models and integrating them forward in time in the gravitational potential computed from the  $N$  bodies and from the point mass representing the black hole. Initial conditions were prepared by re-integrating all orbits with nonzero occupation numbers. The position and velocity of each trajectory were recorded at fixed time intervals; the length of each integration was determined by the orbit’s occupation number. The sense of rotation of the tube orbits was chosen randomly such that the mean motion was everywhere zero. The number of particles was  $2.417 \times 10^6$  for  $\gamma = 1$  and  $2.19 \times 10^5$  for  $\gamma = 2$ ; a smaller  $N$  was chosen for  $\gamma = 2$  since the  $N$ -body integrations were slower for the more condensed model. In addition, more particles were required to resolve the gentler,  $\gamma = 1$  profile.

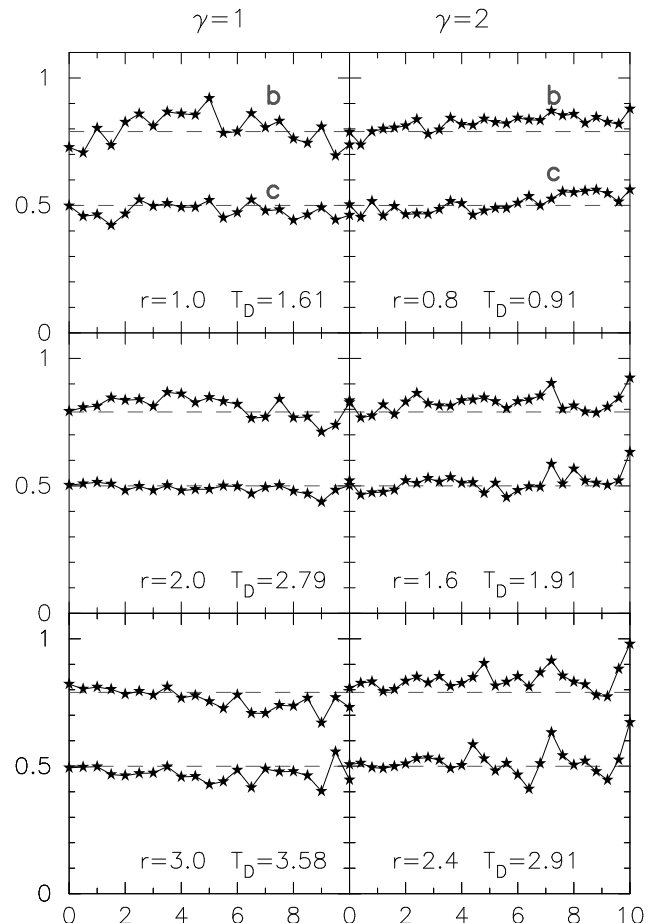


FIG. 2.— Evolution of the  $N$ -body axis ratios;  $a \equiv 1$ .  $r$  defines the longest dimension of the ellipsoid within which the axis ratios were determined, using the algorithm described in the text.  $T_D$  is the dynamical time at this radius.

The initial conditions were then advanced in time using the  $N$ -body code **GADGET** (Springel, Yoshida & White 2001), a tree code with variable time steps. The particle representing the black hole was allowed to move in response to forces from the “stars.” Figure 2 shows the evolution of the axis ratios of the models. Axis ratios were determined using the technique described by Dubinski & Carlberg (1991): the moment of inertia tensor of all particles within an ellipsoid surface  $m = m_o$  is diagonalized; the shape of this surface is then adjusted based on the eigenvalues of the moment of inertia tensor; and the pro-

cedure is iterated until the shape of the surface matches the ellipticity of the particles within the surface. The axis ratios fluctuate with time, but the models retain their triaxial figures very well over many dynamical times. The density profiles of the models also evolve only slightly with time (Figure 3).

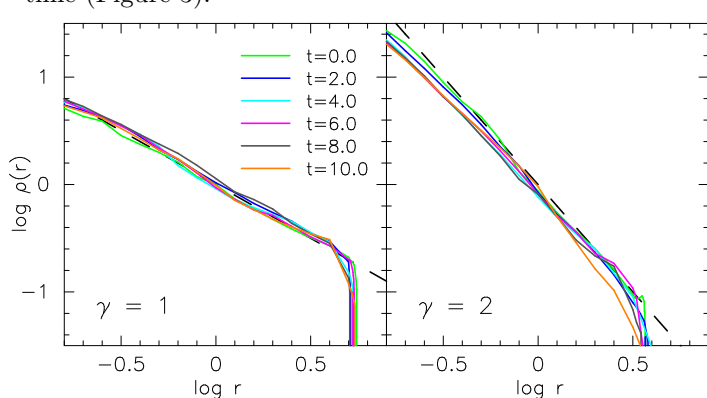


FIG. 3.— Evolution of the density profiles in the  $N$ -body integrations. Dotted lines are the density laws of equation (1).

#### 4. OBSERVABLE PROPERTIES

Two observational signatures of triaxiality are isophote twists, and kinematic misalignments. Isophote twists require a variation with radius of the intrinsic axis ratios, which is not a feature of our models. Kinematic misalignments occur whenever the intrinsic angular momentum vector does not coincide with the minor axis of the figure, and are generic features of triaxial systems when both the short- and long-axis tube orbits are populated (e.g. Franx, Illingworth & de Zeeuw 1991).

We illustrate the possibility of kinematic misalignments in our models in Figure 4. Line-of-sight velocity contours are plotted for each model after a fraction of the  $x$ - and  $z$ -tubes were reversed, giving the models net rotation about both the long and short axes. For  $\gamma = 1$ , all  $x$ -tubes in Figure 4 rotate in the same sense while 60% of the  $z$ -tubes at each energy rotate in one sense and the remaining 40% in the other. For  $\gamma = 2$ , all  $x$ -tubes rotate in the same sense around the  $x$  axis and all  $z$ -tubes rotate in the same sense around the  $z$ -axis. Rotation of the projected models along the apparent minor axis of the figure (“minor-axis rotation”) is clear in Figure 4.

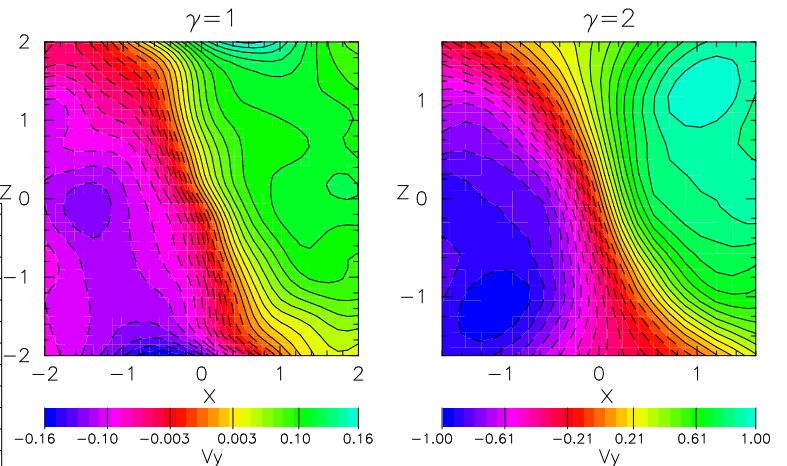


FIG. 4.— Line-of-sight velocities of the rotating models described in the text, as seen along the  $y$ -axis. Contours of positive (negative) velocity are represented by full (dotted) lines.

#### 5. DISCUSSION

Galaxy nuclei are typically modelled as oblate axisymmetric systems when deriving black hole masses from stellar-kinematical data (e.g. van der Marel et al. 1998; Joseph et al. 2001). Modelling a triaxial nucleus as axisymmetric will generally lead to biased estimates of  $M_{bh}$ ; for instance, if an elongated bar is viewed end-on, the velocity field can mimic that produced by a black hole even in the absence of a central mass concentration (Gerhard 1988). The high-resolution data on which such mass estimates are based are usually obtained from single slits, making it difficult to rule out triaxial shapes using information like that in Figure 4.

Axisymmetry is typically also assumed when deriving rates of interaction of stars with nuclear black holes (e.g. Syer & Ulmer 1999; Magorrian & Tremaine 1999). In our triaxial models, most of the orbits were found to be  $z$ -tubes (Table 2), similar to the orbits that populate an oblate spheroid. However much of the mass near the black hole in our  $\gamma = 1$  model was contributed by high-energy box-like orbits, the pyramids, which have no analogs in axisymmetric potentials. A triaxial nucleus constructed from pyramid orbits could experience a much higher rate of interaction of stars with the black hole than an axisymmetric nucleus.

This work was supported by NSF grants AST 96-17088 and 00-71099 and by NASA grants NAG5-6037 and NAG5-9046.

#### REFERENCES

- Crane, P. et al. 1993, *AJ*, 106, 1371
- Dejonghe, H. 1989, *ApJ*, 343, 113
- Dubinski, J. & Carlberg, R. 1991, *ApJ*, 378, 496
- Gebhardt, K. et al. 1996, *AJ*, 112, 105
- Gerhard, O. E. 1988, *MNRAS*, 232, 13p
- Gerhard, O. & Binney, J. J. 1985, *MNRAS*, 216, 467
- Joseph, C. L. et al. 2001, *ApJ*, 550, 668
- Kormendy, J. & Richstone, D. O. 1995, *ARAA*, 33, 581
- Magorrian, J. & Tremaine, S. 1999, *MNRAS*, 309, 447
- Franx, M., Illingworth, G. & de Zeeuw, P. T. 1991, *ApJ*, 383, 112
- Merritt, D. & Fridman, T. 1996, *ApJ*, 460, 136
- Merritt, D. & Quinlan, G. D. 1998, *ApJ*, 498, 625
- Merritt, D. & Valluri, M. 1999, *AJ*, 118, 1177
- Poon, M. Y. & Merritt, D. 2001, *ApJ*, 549, 192 (Paper I)
- Sambhus, N. & Sridhar, S. 2000, *ApJ*, 542, 143
- Schwarzschild, M. 1979, *ApJ*, 232, 236
- Schwarzschild, M. 1982, *ApJ*, 263, 599
- Schwarzschild, M. 1993, *ApJ*, 409, 563
- Sellwood, J. A. 2001, *astro-ph/0107353*
- Springel, V., Yoshida, N. & White, S. D. M. 2001, *NewA*, 6, 79
- Syer, D. & Ulmer, A. 1999, *MNRAS*, 306, 35
- van der Marel, R. P., Cretton, N., de Zeeuw, P. T., Rix, H.-W. 1998, *ApJ*, 493, 613